Fixed Switching Frequency Generalized Peak Current Control (GPCC) of DC–AC Converters

Mohammad Ebrahimi, *Student Member, IEEE*, and S. Ali Khajehoddin, *Senior Member, IEEE*

***Abstract*—A fast and robust fixed switching frequency peak current controller for DC–AC converters is presented. The proposed method tends to mimic the switching behavior of pulse width modulation (PWM) techniques, so it features all the advantages of peak current controllers (such as simplicity, fast transient, and optimum dynamic response), with the superiority of fixed switching frequency and harmonic free output. The proposed method is a generalized approach that can be applied to different PWM schemes. The method is specifically elaborated for single-phase distributed generation applications, using various inverter topologies and mimicking different PWM schemes. Moreover, adaptive bands are proposed to provide active damping for the controller, to extend use of the proposed method for inverters with *LCL* output filters. Feasibility and performance of the controller is shown by means of simulations and experiments.**

***Index Terms*—Current control, dc–ac converters, hysteresis controller, peak current control, single-phase grid-connected inverter.**

I. INTRODUCTION

HYSTERESIS current controller has been a well-known candidate for the control of distributed generation (DG) inverters in renewable energy systems and microgrid applications [1]. Fast transient response, zero tracking error, and inherent maximum current limiting are among the advantages of such controllers [2]–[4]. Hysteresis controllers perfectly mitigate the injection of dc current in DG systems' inverters. Moreover, they can generate pure sinusoidal currents in highly distorted grid voltage conditions, with no need for additional control actions. These controllers also provide good large-signal response and stability [5].

As the output is strictly controlled within upper and lower bands, switching frequency of the hysteresis current controllers varies over a fundamental cycle and is susceptible to the operating point and system parameters [2], [6]. This leads to undesired and unpredictable harmonic spectrum of the inverters' output and difficulties in design of the output ac and EMI filters. On the contrary, peak current controllers are proposed that control the output current by comparing only the maximum (or minimum) of the current with a band to generate the OFF (or ON) signal of the inverter switches. Therefore, unlike the hysteresis controller, only one band is used and a clock signal complements the switching command in each switching cycle. Consequently, a fixed switching frequency is obtained, but features like zero tracking error and inherent current limiting are lost [7]. Moreover, an instability exists for peak current controllers [8] that requires a slope compensation strategy for the current band [9], [10], which adds to the complexity of the method.

In the existing peak or hysteresis current control methods, the modulation is not the same as any known pulse width modulation (PWM) scheme. Therefore, harmonic spectrum and the converters' performance are not predictable. Besides, extensive research has been done on PWM switching scheme and several approaches are proposed to achieve different characteristics for the PWM-controlled inverters [11], [12]. However, there is no link between these PWM strategies and existing peak current controllers, and thus, extensive knowledge of these PWM schemes cannot be used in the hysteresis or peak current-controlled inverters.

Several methods are proposed to address some of the aforementioned limitations and problems. Some methods have tried to synchronize the switching action of the hysteresis current controller to an external clock signal. For example, in one approach, bands of the controller are determined based on the output of a phase-locked loop (PLL), which tries to lock the inverters' switching action to a reference clock [13]. This method employs some filtering actions in the calculation of the bands, which are reported to initiate stability problems and also the PLL synchronization will be lost in large output transients. This method is improved in [14] by replacing the PLL with a predictive band calculation method. In this approach, the external clock is used to calculate inverter bands for the next clock cycle, based on slope of the output current in previous cycle. Although they achieve a nearly constant switching frequency, all these methods are complicated and their dynamic performance is degraded, compared to the traditional hysteresis current controllers.

In another approach [15], current bands are adjusted to provide a fixed switching frequency for the inverter. Several research studies have applied the method proposed in [15] to the grid-connected inverter applications [16], [17]. Although these methods achieve a nearly constant switching frequency, their application in DG inverters and the related issues such as resonance damping of the LCL filter are not studied. Moreover, none of them claim to generate any known PWM scheme and as a result, design of the system for electromagnetic interference (EMI), electromagnetic compatibility (EMC), or loss calculation are not possible, and the performance for special cases such as controlling leakage current in photovoltaic (PV) sys-

---

Manuscript received June 6, 2016; revised September 3, 2016; accepted October 10, 2016. Date of publication October 25, 2016; date of current version March 24, 2017. Recommended for publication by Associate Editor D. Vinnikov.

The authors are with the Department of Electrical and Computer Engineering, University of Alberta, Edmonton T6G 1H9, Canada (e-mail: m.ebrahimi@ualberta.ca; khajeddin@ualberta.ca).

Color versions of one or more of the figures in this paper are available online at http://ieeexplore.ieee.org.

Digital Object Identifier 10.1109/TPEL.2016.2620976

tem [18] is not predictable or controllable. Moreover, none of these studies have addressed a comprehensive solution that can be extended to topologies other than the H-bridge converter, and interfacing filters other than a simple inductor. In another method [19], the concept of adaptive current bands is combined with the approach of synchronizing to an external clock. In this method, switching timings are calculated such that the current remains within its predefined bands. Although it guarantees a fixed switching frequency, this method does not directly control peak value of the current, and thus, its transient response is degraded and cannot operate as a current limiting method.

A simple but effective approach is presented in this paper, which benefits advantages of hysteresis and peak current controllers to provide both zero steady-state error and fixed switching frequency with a predictable harmonic spectrum. The proposed method achieves the following objectives: 1) the link between hysteresis current control of the inverter and existing PWM schemes is elaborated, which features the advantages of both methods in the resulting controller; 2) the approach is proved to be extendable to different inverter topologies such as multilevel and Z-source converters, and different PWM schemes; and 3) the method is proposed for a general case of a grid-connected inverter with an *L* filter, and subsequently, is extended to higher order *LCL* output filter configurations. Additional control objectives such as active damping of the output filter are also investigated.

This paper is organized as follows. In Section II, the proposed method is described and the general rules of achieving current bands for different switching schemes are elaborated. This method is applied to well-known unipolar and bipolar PWM schemes, and multilevel and Z-source converters in Section III. Application of the proposed method for single-phase DG systems with higher order output filters and active damping is investigated in Section IV. In Section V, feasibility of the proposed method and performance of the proposed damping approach are shown by simulations and experimental results. This paper is concluded in Section VI.

II. GENERALIZED PEAK CURRENT CONTROL METHOD

The proposed approach is inspired by the basic operation principle of the PWM technique. PWM-controlled inverters present a clean output harmonic spectrum, which is a result of their fixed switching frequency. Moreover, several PWM schemes are proposed in the literature to provide different output switching characteristics for an inverter [18]. The proposed controller aims to achieve the desired output spectrum of a PWM-controlled inverter with a peak current control strategy. This technique is called generalized peak current control (GPCC) as it can be applied to different types of PWMs and different inverter topologies, resulting in a family of peak current controllers maintaining their original PWM features. As a result, all advantages of the peak current controllers, such as fast dynamic response, inherent overcurrent protection, and direct control on the instantaneous value of the inverter current are inherited along with clean predictable harmonic spectrum, constant switching frequency, and additional desired output characteristics of the original PWM.

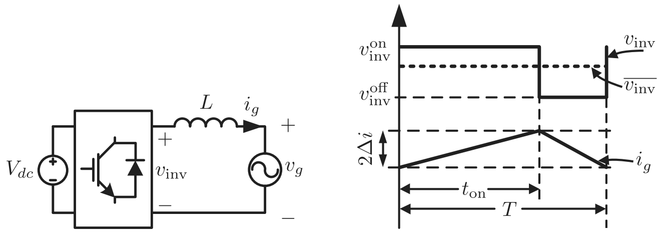

(a) (b)

Fig. 1. (a) Typical grid-connected inverter with an *L* filter. (b) Sample of the inverters' output voltage and current for one switching cycle.

The main idea is that if a known PWM scheme generates specific peak current envelopes, we can achieve a similar switching action by controlling the current within the same current envelopes. To exactly mimic a given PWM, first the current envelop for an inverter using that PWM signal is derived. An inverter connected to the grid through an *L* filter is shown in Fig. 1(a). Regardless of the inverters' topology and PWM scheme, its output voltage and current have the form of Fig. 1(b). This inverter is assumed to be controlled by a PWM, so it has a known desirable output voltage spectrum with a constant switching frequency. In this figure, T is the inverters' effective output switching period that could be different from the PWM carrier signal period, T_s, depending on the inverter topology and its PWM. As per Fig. 1(b), $\overline{v_{\mathrm{inv}}}$ is the average of inverter output voltage v_{inv} during one period T, where the moving average operator is denoted by the overbar and is defined as $\overline{x} = \int_{t-T}^{t} x(\tau)d\tau$.

As the effective switching frequency $\frac{1}{T}$ is assumed to be much higher than the fundamental frequency, just the switching ripple of the current is taken into consideration and other parameters are assumed to be constant during each switching cycle. Accordingly, if $\overline{v_{\mathrm{inv}}}$ is known, t_{on} can be calculated from $\overline{v_{\mathrm{inv}}} = \frac{1}{T}\left(v_{\mathrm{inv}}^{\mathrm{on}} t_{\mathrm{on}} + v_{\mathrm{inv}}^{\mathrm{off}}(T - t_{\mathrm{on}})\right)$ as

$$t_{\mathrm{on}} = T\frac{\overline{v_{\mathrm{inv}}} - v_{\mathrm{inv}}^{\mathrm{off}}}{v_{\mathrm{inv}}^{\mathrm{on}} - v_{\mathrm{inv}}^{\mathrm{off}}}. \tag{1}$$

Moreover, $v_{\mathrm{inv}}^{\mathrm{on}}$ determines the voltage drop across the filter inductance L. As a result, the current band will be specified for each switching cycle as $2\Delta i = \frac{1}{L}(v_{\mathrm{inv}}^{\mathrm{on}} - v_g)t_{\mathrm{on}}$, i.e.

$$\Delta i = \frac{T}{2L}\frac{\left(v_{\mathrm{inv}}^{\mathrm{on}} - v_g\right)\left(\overline{v_{\mathrm{inv}}} - v_{\mathrm{inv}}^{\mathrm{off}}\right)}{v_{\mathrm{inv}}^{\mathrm{on}} - v_{\mathrm{inv}}^{\mathrm{off}}}. \tag{2}$$

It is worth mentioning that depending on the inverter topology and the PWM scheme, v_{inv} may have to be divided into different regions. For example, in a single-phase H-Bridge inverter controlled with a unipolar PWM scheme, v_{inv} changes from 0 to $+V_{\mathrm{dc}}$ for $\overline{v_{\mathrm{inv}}} \geq 0$, and from $-V_{\mathrm{dc}}$ to 0 when $\overline{v_{\mathrm{inv}}} < 0$. Therefore, Δi has two different values for these two regions.

The calculated current bands are then used to control the current in a peak current controller. Accordingly, switching states of the inverter are determined such that an output harmonic spectrum similar to the original PWM controller is achieved. In the next section, the GPCC method is derived for different switching schemes and different inverter topologies such as a simple H-Bridge inverter and a more complicated multilevel neutral-point clamped (NPC) inverter and a Z-source converter.

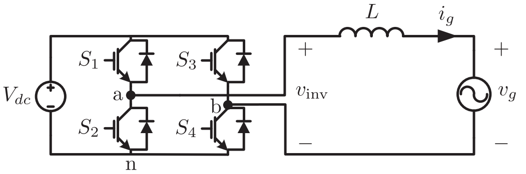

Fig. 2. Single-phase H-bridge inverter interfaced with the grid through an L filter.

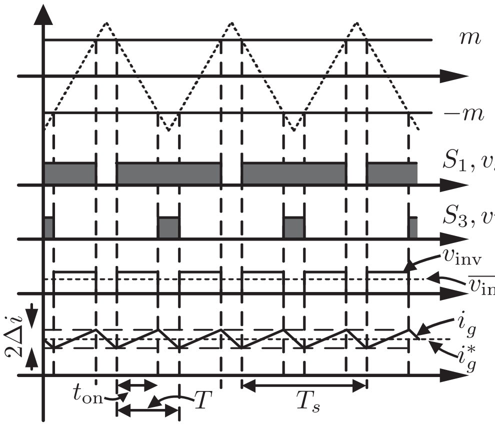

Fig. 3. Operation principle of the inverter controlled with unipolar PWM scheme for $\overline{v_{\rm inv}} \geq 0$ or equally $m \geq 0$.

III. DERIVING THE GPCC CURRENT BANDS

A. GPCC Mimicking Unipolar PWM Scheme

1) Formulation: The circuit diagram of a single-phase inverter interfaced to the grid through an L filter is shown in Fig. 2. Key waveforms of this inverter for the case $\overline{v_{\rm inv}} \geq 0$ is shown in Fig. 3. In this figure, modulation index m is defined as $m = \overline{v_{\rm inv}}/V_{\rm dc}$. Signal m is compared with the carrier waveform to generate the switching signal for switch S_1. In a unipolar PWM scheme, leg a of the inverter is controlled with m, and leg b is controlled with $-m$ signal.

Regarding Fig. 2 and assuming a sinusoidal grid voltage as $v_g = \widehat{V}_g \sin(\omega t)$ and a grid current such as $i_g^* = \widehat{I}^* \sin(\omega t)$, $\overline{v_{\rm inv}}$ will be

$$\begin{aligned} \overline{v_{\rm inv}} &= \widehat{V}_{ab}\sin(\omega t + \delta) \\ \widehat{V}_{ab} &= \sqrt{\left(\omega L \widehat{I}^*\right)^2 + \left(\widehat{V}_g\right)^2} \quad , \quad \delta = \tan^{-1}\left(\frac{\omega L \widehat{I}^*}{\widehat{V}_g}\right). \end{aligned} \tag{3}$$

Fig. 3 shows the switching signals for the two upper switches S_1 and S_3 and it can be observed that effective output switching frequency of unipolar PWM inverter is $2f_s$ ($f_s = 1/T_s$). In this configuration, $v_{\rm inv}$ has two different regions in terms of values of $v_{\rm inv}^{\rm off}$ and $v_{\rm inv}^{\rm on}$ and hence, $t_{\rm on}$ and Δi have to be calculated for $\overline{v_{\rm inv}} \geq 0$ and $\overline{v_{\rm inv}} < 0$, separately. Considering (2) with $T = T_s/2$, Δi is obtained as

$$\Delta i = \begin{cases} \dfrac{T_s/2}{2L}\dfrac{(V_{\rm dc} - v_g)(\overline{v_{\rm inv}})}{V_{\rm dc}}, & \overline{v_{\rm inv}} \geq 0 \\[2ex] \dfrac{T_s/2}{2L}\dfrac{(-V_{\rm dc} - v_g)(\overline{v_{\rm inv}})}{-V_{\rm dc}}, & \overline{v_{\rm inv}} < 0. \end{cases} \tag{4}$$

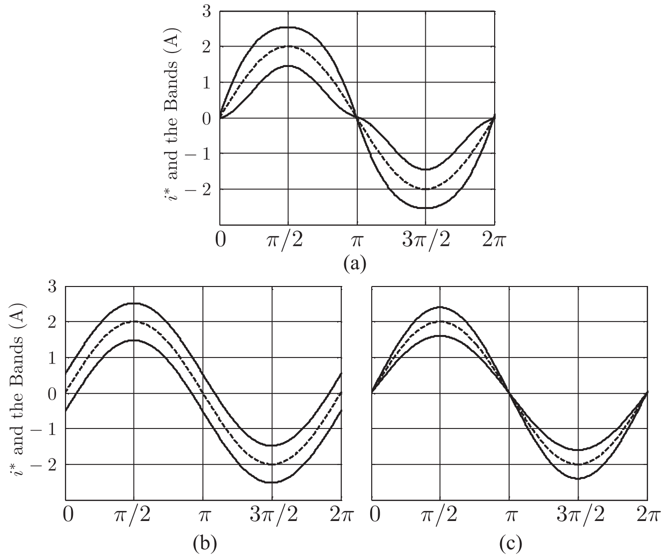

(a)

(b)

(c)

Fig. 4. Comparison of the current bands for the proposed GPCC with the conventional methods. (a) The proposed method (b) Conventional Fixed-band (c) Conventional Sine-band.

Combining this equation with (3) results in the current bands as

$$\Delta i = \begin{cases} \dfrac{T_s}{4L}\dfrac{\left(V_{\rm dc} - \widehat{V}_g\sin(\omega t)\right)\left(\widehat{V}_{ab}\sin(\omega t + \delta)\right)}{V_{\rm dc}}, & \overline{v_{\rm inv}} \geq 0 \\[2ex] \dfrac{T_s}{4L}\dfrac{\left(V_{\rm dc} + \widehat{V}_g\sin(\omega t)\right)\left(\widehat{V}_{ab}\sin(\omega t + \delta)\right)}{V_{\rm dc}}, & \overline{v_{\rm inv}} < 0. \end{cases} \tag{5}$$

The aforementioned equation calculates the peak value of the grid current for the inverter of Fig. 2 with a unipolar PWM. Therefore, if the same equations are used to generate a variable current band, a constant-frequency switching pattern will be obtained, which mimics the switching action of the unipolar PWM. This is contrary to the conventional peak current controller where the bands are either fixed or sinusoidal [20], generating a variable switching frequency. The proposed and the conventional bands are compared in Fig. 4. Simulations confirm that the switching frequency of the conventional Sine-band and fixed-band hysteresis controllers changes over a fundamental cycle from 39.8 to 20 kHz and 14 to 20 kHz, respectively. This is while the proposed GPCC achieves a very small variation in the output switching frequency from 19.2 to 20 kHz in the same testing condition.

It is worth mentioning that maximum amount of Δi obtained from (5) also significantly helps for the optimum magnetic design of the filter inductor.

2) Reactive Power Control: This controller is also extended to regulate the reactive power. For a general case of a nonunity power factor, the grid current is assumed in the form of $i_g^* = \widehat{I}^* \sin(\omega t - \varphi)$, where $\cos(\varphi)$ is the power factor at the inverters' output. Accordingly, $\overline{v_{\rm inv}}$ will be

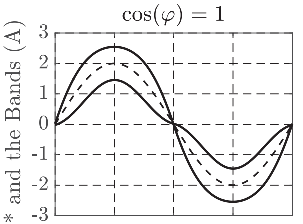

Fig. 5. Upper and lower current bands for two different power factors, $\cos(\varphi) = 1$ and $\cos(\varphi) = 0.5$.

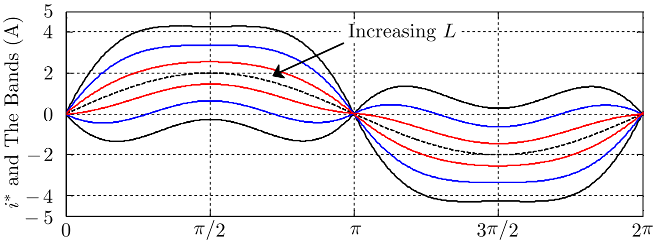

Fig. 6. Upper and lower current bands for different filter inductance values in the proposed GPCC.

calculated as

$$\begin{aligned}\overline{v_{\rm inv}} &= \widehat{V}_{ab}\sin\left(\omega t+\delta\right)\\ \widehat{V}_{ab} &= \sqrt{\left(\omega L\widehat{I}^*\cos(\varphi)\right)^2+\left(\widehat{V}_g+\omega L\widehat{I}^*\sin(\varphi)\right)^2}\\ \delta &= \tan^{-1}\left(\frac{\omega L\widehat{I}^*\cos(\varphi)}{\widehat{V}_g+\omega L\widehat{I}^*\sin(\varphi)}\right).\end{aligned}\tag{6}$$

Using this adjusted $\overline{v_{\rm inv}}$, current bands of (5) will be used to control the desired active and reactive power. Current bands of the controller for $\cos(\varphi) = 1$ and $\cos(\varphi) = 0.5$ are shown in Fig. 5, where the apparent power S is kept constant for both cases. It will be shown in Section V that these two different bands will provide a similar output harmonic spectrum for the inverter as they regulate the desired output power.

3) Effect of Inductance L on Current Bands: Current bands of the proposed technique are also sketched for different values of the filter inductance in Fig. 6, where each color shows the upper and lower bands for each inductor value. This figure clearly shows the effect of inductance value and the double frequency term on the current bands.

Considering the current band formulas [in (5)] along with $\widehat{V}_{ab}$ and δ definitions, sensitivity of Δi toward different variables can be assessed. Having $V_{\rm dc}$ and v_g as the feedback, Δi just depends on the inductor value, L. Assume that current bands are calculated for a given filter inductance and the inverter is then controlled based on these calculated bands. In this case, if the inverter faces some mismatch in the design value of L compared to its actual value, then the switching frequency will be slightly different from the expected value. Rearranging (5) shows that switching frequency of the inverter is inversely proportional to the amount of actual L, that is $f_s = \frac{1}{T_s} \propto \frac{1}{L}$. Therefore, if L slightly deviates from its designed value, output harmonic spectrum of the inverter remains similar to the original PWM scheme, with a slightly different switching frequency. If the frequency variation is important, one can adaptively change L in (5) to have the frequency absolutely constant.

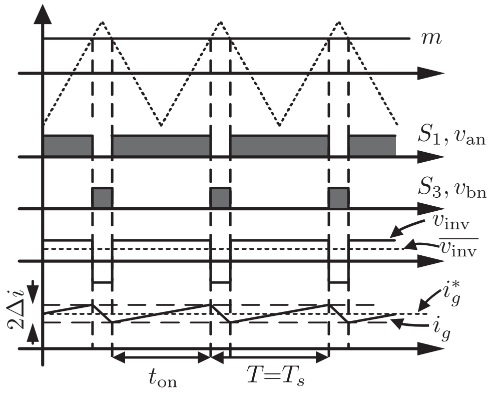

Fig. 7. Operation principle of the inverter controlled with the bipolar PWM scheme.

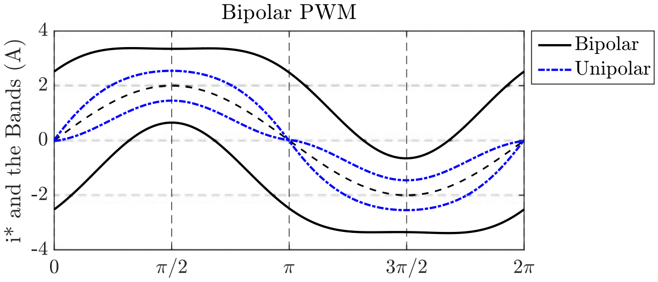

Fig. 8. Current bands for the proposed GPCC based on the bipolar PWM switching scheme and its comparison with unipolar PWM.

B. GPCC Mimicking Bipolar PWM Scheme

Key waveforms for the single-phase inverter of Fig. 2 controlled with bipolar PWM is presented in Fig. 7. In the bipolar scheme, diagonal switch pairs $\{S_1, S_4\}$ and $\{S_3, S_2\}$ are controlled with the same switching signals. Following the procedure of obtaining the current bands, $t_{\rm on}$ can be calculated from (1) and Δi from (2) as

$$t_{\rm on} = T_s\frac{\overline{v_{\rm inv}}+V_{\rm dc}}{2V_{\rm dc}}\tag{7}$$

$$\Delta i = \frac{T_s}{4L}\frac{\left(V_{\rm dc}-v_g\right)\left(\overline{v_{\rm inv}}+V_{\rm dc}\right)}{V_{\rm dc}}.\tag{8}$$

Fig. 8 presents the current band of GPCC mimicking bipolar PWM. Also these bands are compared with those of unipolar PWM for the same filter inductance value. As it can be observed, mimicking bipolar PWM results in much larger switching ripples to maintain the same switching frequency as unipolar PWM. This is because the effective switching frequency in bipolar PWM is half of the value for unipolar PWM. However, bipolar PWM achieves better results in elimination of ground leakage current in PV inverter application, since it does not generate any common-mode voltage at the inverters' output [18].

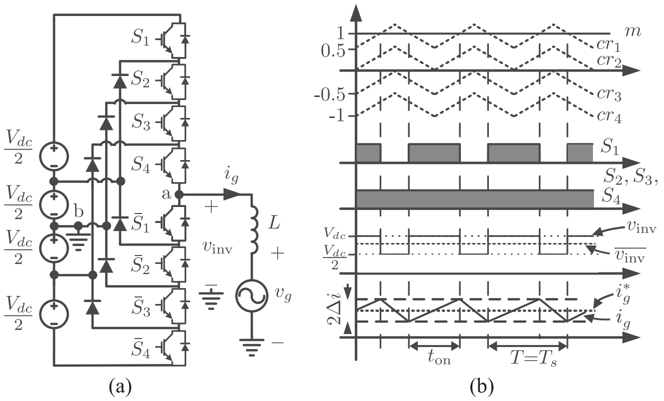

(a) (b)

Fig. 9. Five-level NPC converter. (a) Circuit diagram, (b) key waveforms when controlled with IPD modulation.

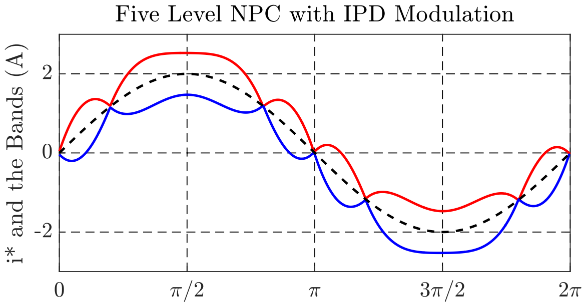

Fig. 10. GPCC current bands derived based on the IPD modulation for the five-level NPC converter.

C. GPCC For Multilevel Converters

The GPCC can be applied to different modulation schemes that are proposed to control multilevel converters. The circuit diagram of a five-level half-bridge NPC converter is depicted in Fig. 9(a). Key waveforms of applying a level-shifted PWM such as in-phase disposition (IPD) modulation [21] to this converter are shown in Fig. 9(b).

The GPCC can control such multilevel converter, mimicking the switching behavior of original IPD modulation. In the case of a five-level NPC, v_{inv} has four different regions in terms of values of $v_{\text{inv}}^{\text{on}}$ and $v_{\text{inv}}^{\text{off}}$. Accordingly, (2) is used to achieve current bands for each of these regions as

$$\Delta i = \begin{cases} \frac{T_s}{2L}\left(V_{\text{dc}} - v_g\right)\left(2\frac{\overline{v_{\text{inv}}}}{V_{\text{dc}}} - 1\right) & \frac{V_{\text{dc}}}{2} \le \overline{v_{\text{inv}}} < V_{\text{dc}} \\ \frac{T_s}{2L}\left(\frac{V_{\text{dc}}}{2} - v_g\right)\left(2\frac{\overline{v_{\text{inv}}}}{V_{\text{dc}}}\right) & 0 \le \overline{v_{\text{inv}}} < \frac{V_{\text{dc}}}{2} \\ \frac{T_s}{2L}\left(\frac{V_{\text{dc}}}{2} + v_g\right)\left(2\frac{\overline{v_{\text{inv}}}}{V_{\text{dc}}}\right) & -\frac{V_{\text{dc}}}{2} \le \overline{v_{\text{inv}}} < 0 \\ \frac{T_s}{2L}\left(V_{\text{dc}} + v_g\right)\left(2\frac{\overline{v_{\text{inv}}}}{V_{\text{dc}}} + 1\right) & -V_{\text{dc}} \le \overline{v_{\text{inv}}} < -\frac{V_{\text{dc}}}{2}. \end{cases} \tag{9}$$

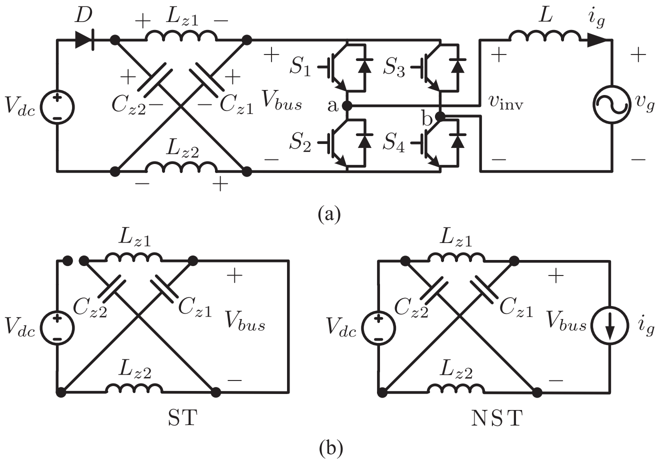

Fig. 11. Z-source H-bridge inverter. (a) Circuit diagram, (b) equivalent circuit for ST and NST modes of operation.

Resulting bands are shown in Fig. 10 and as it can be observed, output current also has four regions corresponding to different levels of inverters' output voltage.

The GPCC can be applied to a general case of a N-level NPC converter, where Δi has $N-1$ regions. Current bands are given in (10) for $\overline{v_{\text{inv}}} \ge 0$ (top equation) and $\overline{v_{\text{inv}}} < 0$ (bottom equation), where J is defined as $J = \frac{N-1}{2}$.

$$\Delta i = \begin{cases} \frac{T_s}{2L}\left(k\frac{V_{\text{dc}}}{J} - v_g\right)\left(J\frac{\overline{v_{\text{inv}}}}{V_{\text{dc}}} - (k-1)\right), \\ \qquad \frac{k-1}{J}V_{\text{dc}} \le \overline{v_{\text{inv}}} < \frac{k}{J}V_{\text{dc}} \\ \frac{T_s}{2L}\left(-k\frac{V_{\text{dc}}}{J} - v_g\right)\left(J\frac{\overline{v_{\text{inv}}}}{V_{\text{dc}}} + (k-1)\right), \\ \qquad -\frac{k}{J}V_{\text{dc}} \le \overline{v_{\text{inv}}} < -\frac{k-1}{J}V_{\text{dc}} \end{cases}$$

$$k = \{1, 2, \ldots, J\}. \tag{10}$$

Note that as single-phase half-bridge NPC converters use the dc bus midpoint as the grid current return path, N has to be an odd number.

D. GPCC Bands for Impedance Source Inverters With Shoot-Through State

The circuit diagram of a single-phase H-bridge impedance-(Z-) source inverter [22] is shown in Fig. 11(a). Adding a shoot-through (ST) state in which both upper and lower switches of the inverter leg are turned ON simultaneously will introduce a buck–boost characteristic to the Z-source inverter. Accordingly, the equivalent circuits of Fig. 11(b) are considered for the ST and nonshoot-through (NST) states [22].

Principle of operation of the Z-source inverter controlled with bipolar PWM and ST states is depicted in Fig. 12. To implement the ST states, a bias equal to $m_0/2$ is added to the modulation index m, generating the switching commands S_1 and S_4. To keep the positive and negative voltage balance at the output of the inverter unchanged, bias $m_0/2$ is also deducted from the

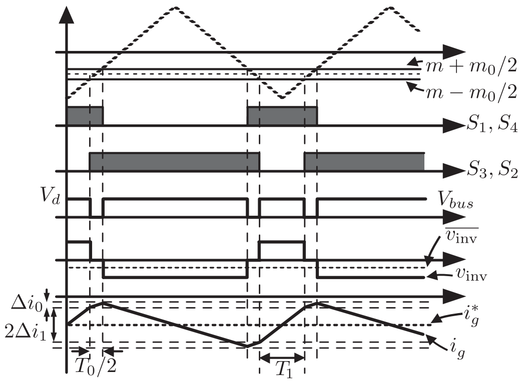

Fig. 12. Grid-connected Z-source inverter principle of operation.

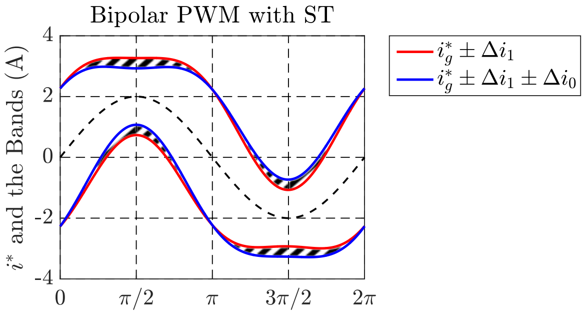

Fig. 13. current bands of the Z-source inverter mimicking bipolar PWM with $m_0 = 0.2$.

modulation index m to generate switching signals S_3 and S_2. Consequently, a total ST state m_0 equal to the total time T_0 is implemented in each switching cycle.

Assuming that the Z network is symmetrical, i.e., $V_{Cz1} = V_{Cz2} = V_{Cz}$ and $V_{Lz1} = V_{Lz2} = V_{Lz}$, V_{bus} voltage is calculated as [22]

$$\begin{aligned} \text{ST}: \quad & V_{\text{bus}} = 0 \\ \text{NST}: \quad & V_{\text{bus}} = V_d = 2V_{Cz} - V_{\text{dc}}. \end{aligned} \tag{11}$$

Also the capacitor voltage is calculated by having the average inductor voltage across one switching cycle equal to zero, hence

$$V_{Cz} = \left(\frac{T_s - T_0}{T_s - 2T_0}\right) V_{\text{dc}}.$$

Note that $T_0/T_s = m_0/2$, so the aforementioned equation can be rewritten as

$$V_{Cz} = \left(\frac{1 - \frac{m_0}{2}}{1 - m_0}\right) V_{\text{dc}}. \tag{12}$$

According to Fig. 12, $T_1 = t_{\text{on}} - T_0/2$, thus regarding (2) by adjusting the average inverter voltage as $\overline{v_{\text{inv}}} - \frac{m_0}{2} V_d$ to correspond with the ST duration, Δi_1 is calculated as (13). With the same approach, Δi_0 is also calculated.

$$\begin{aligned} \Delta i_1 &= \frac{T_s}{4L} \frac{(V_d - v_g)\left(\left(\overline{v_{\text{inv}}} - \frac{m_0}{2} V_d\right) + V_d\right)}{V_d} \\ \Delta i_0 &= \frac{T_s}{4L} \left(-m_0 v_g\right). \end{aligned} \tag{13}$$

It is worth mentioning that by omitting the ST state, i.e., $m_0 = 0$, Δi_1 in the aforementioned equation becomes the same as (8) and Δi_0 goes to zero. Therefore, the bands become exactly those of the GPCC mimicking a regular bipolar PWM and the Z-source inverters' dc voltage gain equals unity, i.e., $V_d = V_{\text{dc}}$. Current bands of (13) are depicted in Fig. 13 for $m_0 = 0.2$. When i_g is within the two upper or the two lower bands, that is in the hatched area, the inverter is in the ST state and switching action is accordingly determined. Note that V_d in (13) can be calculated based on the feedback from V_{dc} and V_{Cz}, to account for the system uncertainties.

With the same approach, the GPCC can be applied to different inverter topologies and to various PWM schemes with ST states proposed for the control of impedance source inverters [23].

In addition, based on conditions such as the operating point, Z-source inductance value, and etc., some other modes of operation are possible for a Z-source inverter. These additional unwanted modes are investigated in [24] and are not considered here as they are beyond the scope of this paper. However, one can apply the preceding analysis to those modes as well, either in its exact form or by some sort of approximations.

As presented in this section, the proposed GPCC can be applied to different converter topologies and can mimic different PWM schemes. Summary of controller equations derived in this section is provided in Table I.

IV. EXTENSION OF THE GPCC FOR *LCL* TYPE FILTERS

The circuit diagram of the single-phase DG inverter with an *LCL* filter is depicted in Fig. 14(a). Although the *LCL* filter features an effective filtering action at a smaller size, it will introduce an undesired resonant oscillation to the output current. The proposed approach in this section adaptively adjusts the bands in the peak current controller, to actively damp the undesired resonance of the *LCL* filter.

A. *Control Structure and Feedback Selection*

PWM inverters control the average value of output grid current indirectly, by controlling output voltage of the inverter. Therefore, as shown in Fig. 14(b) they can be modeled as a voltage source, connected to the grid through an *LCL* filter. On the contrary, peak current controllers directly control peak value of the inductor current. Therefore, if the inductor L current (i_i) is selected as the feedback variable, an inverter can be modeled as a current source connected to the rest of the circuit as shown in Fig. 14(c). As i_i is tightly controlled, its dynamic does not contribute in the undesired resonance of the output, and only L_g and C will resonate with each other. If capacitor voltage (v_c) is selected as the voltage feedback, current bands derived in Section III for the simple L filter case will be still valid by substitution of v_g by v_c. As discussed later in this section, this configuration provides the opportunity for active damping of the resonance with no need for additional sensors.

TABLE I
GPCC CURRENT BANDS

	T	$v_{\mathrm{inv}}^{\mathrm{on}}$	$v_{\mathrm{inv}}^{\mathrm{off}}$	Δi	
General Case	T	$v_{\mathrm{inv}}^{\mathrm{on}}$	$v_{\mathrm{inv}}^{\mathrm{off}}$	$\frac{T}{2L}\frac{\left(v_{\mathrm{inv}}^{\mathrm{on}}-v_g\right)\left(\overline{v_{\mathrm{inv}}}-v_{\mathrm{inv}}^{\mathrm{off}}\right)}{v_{\mathrm{inv}}^{\mathrm{on}}-v_{\mathrm{inv}}^{\mathrm{off}}}$	-
Unipolar PWM	$2T_s$	V_{dc}	0	$\frac{T_s}{4L}\frac{\left(V_{\mathrm{dc}}-\widehat{V}_g\sin(\omega t)\right)\left(\widehat{V}_{ab}\sin(\omega t+\delta)\right)}{V_{\mathrm{dc}}}$	$\overline{v_{\mathrm{inv}}}\geq 0$
		$-V_{\mathrm{dc}}$	0	$\frac{T_s}{4L}\frac{\left(V_{\mathrm{dc}}+\widehat{V}_g\sin(\omega t)\right)\left(\widehat{V}_{ab}\sin(\omega t+\delta)\right)}{V_{\mathrm{dc}}}$	$\overline{v_{\mathrm{inv}}}< 0$
Bipolar PWM	T_s	V_{dc}	$-V_{\mathrm{dc}}$	$\frac{T_s}{4L}\frac{\left(V_{\mathrm{dc}}-v_g\right)\left(\overline{v_{\mathrm{inv}}}+V_{\mathrm{dc}}\right)}{V_{\mathrm{dc}}}$	-
IPD PWM	T_s	$k\frac{V_{\mathrm{dc}}}{J}$[a]	$\frac{(k-1)V_{\mathrm{dc}}}{J}$	$\frac{T_s}{2L}\left(k\frac{V_{\mathrm{dc}}}{J}-v_g\right)\left(J\frac{\overline{v_{\mathrm{inv}}}}{V_{\mathrm{dc}}}-(k-1)\right)$	$\frac{k-1}{J}V_{\mathrm{dc}}\leq\overline{v_{\mathrm{inv}}}<\frac{k}{J}V_{\mathrm{dc}}$
		$-k\frac{V_{\mathrm{dc}}}{J}$	$-\frac{(k-1)V_{\mathrm{dc}}}{J}$	$\frac{T_s}{2L}\left(-k\frac{V_{\mathrm{dc}}}{J}-v_g\right)\left(J\frac{\overline{v_{\mathrm{inv}}}}{V_{\mathrm{dc}}}+(k-1)\right)$	$-\frac{k}{J}V_{\mathrm{dc}}\leq\overline{v_{\mathrm{inv}}}<-\frac{k-1}{J}V_{\mathrm{dc}}$

[a] N level converter: $J=\frac{N-1}{2}$ and $k=\{1,2,\ldots,J\}$.

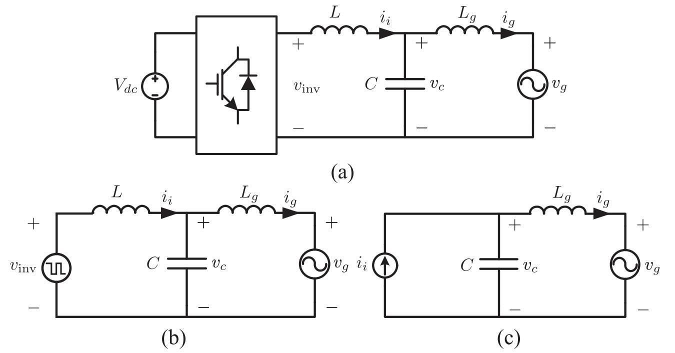

(a)

(b)

(c)

Fig. 14. Single-phase inverter connected to the grid through an *LCL* filter. (a) Circuit diagram. (b) PWM-controlled inverter circuit diagram. (c) Simplified model for a peak current-controlled inverter.

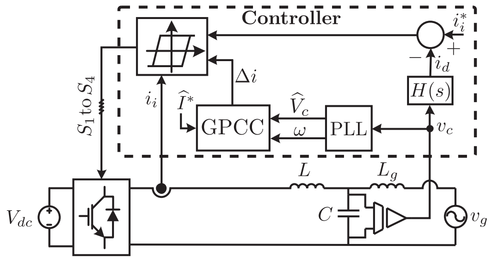

Fig. 15. Block diagram of the proposed controller along with the cost-effective active resonant damping technique.

B. Resonant Damping Strategy

Fig. 15 shows a detailed block diagram of an inverter and the extended GPCC with the proposed damping scheme. A synchronization unit such as enhanced PLL [25] or second-order generalized integrator PLL [26] is utilized to provide the grid voltage amplitude and phase angle for the GPCC.

The branch of i_d in Fig. 15 shows the proposed damping structure, which affects upper and lower bands of the controller to provide active damping for the system. i_d is generated using $H(s)$ as

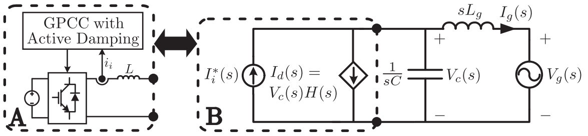

Fig. 16. Equivalent circuit combining the proposed active damping technique with a simplified model of the power circuit.

$$H(s)=\frac{I_d(s)}{V_c(s)}=\frac{k\omega_c^2 s}{s^2+2\zeta\omega_c s+\omega_c^2} \tag{14}$$

where ω_c and ζ are cutoff frequency and damping ratio of the $H(s)$ low-pass filtering action. Using the simplified model of Fig. 14(c) and considering the proposed active damping branch for this model (as per Fig. 15), an equivalent circuit can be sketched as shown in Fig. 16. In this figure, the inverter along with its controller, shown in the dotted box A, are substituted with the dotted box B. Since the current in the inductor L is directly controlled through the GPCC, it is replaced with equivalent current sources, including the active damping branch. Accordingly, $I_g(s)=I_i^*(s)-H(s)V_c(s)-sCV_c(s)$ and $V_c(s)=V_g(s)+sL_gI_g(s)$, hence, transfer functions of $G_i(s)=\frac{I_g(s)}{I_i^*(s)}$ and $G_y(s)=\frac{I_g(s)}{V_g(s)}$ can be easily obtained, which are then used to design the parameter k in (14).

Bode diagrams of $G_i(s)$ and $G_y(s)$, for $\zeta=0.707$ and $\omega_c=2\pi\times 5000$ rad/s (that is chosen to be around the resonant frequency) are shown in Fig. 17. This figure confirms that when the active damping branch is disabled in the controller ($k=0$ graphs), both $G_i(s)$ and $G_y(s)$ have resonant peaks. This resonant is taking place at $1/(2\pi\sqrt{L_gC})\approx 5$ kHz. This verifies previous discussion about the fact that L does not participate in the output resonance (unlike a PWM-controlled inverter), as its current is tightly controlled.

By activating the proposed active damping technique, it is shown in Fig. 17 that different k values change $G_i(s)$ and $G_y(s)$ characteristics. As it can be observed, $k=0.01C$ does not effec-

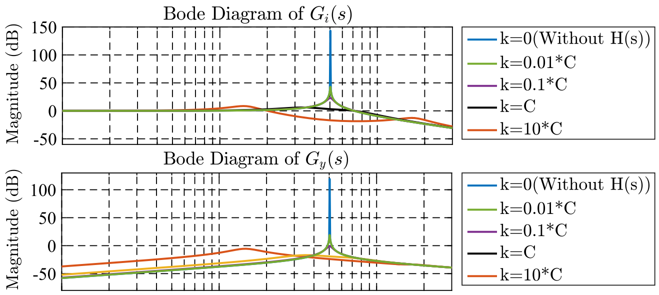

Fig. 17. Bode diagrams of $G_i(s)$ and $G_y(s)$ transfer functions for different k values ($\omega_c = 10^4\pi$ rad/s and $\zeta = 0.707$).

TABLE II
SYSTEM PARAMETERS

DC-link voltage	V_{dc}	200 V
Grid RMS voltage	V_g	120 V
Grid angular frequency	ω	$2\pi \times 60$ rad/s
Switching period	T_s	10^{-4} s
Filter parameters	L	2 mH
	L_g	0.5 mH
	C	2 μF
$H(s)$ parameters	ω_c	$2\pi \times 5000$ rad/s
	k	2×10^{-6}
	ζ	0.707

tively damp the output resonance, while $k = 10C$ totally affects the resonant peak. However, larger values of k also increase the low-frequency gain of $G_y(s)$, which is undesired as it makes the grid current more susceptible to the grid voltage. Therefore, $k = C$ is selected as the $H(s)$ gain, which gives an effective damping for resonance of the system without much changing the low-frequency behavior of $G_y(s)$.

V. PERFORMANCE ANALYSIS

Performance of the proposed GPCC is evaluated by means of simulations and experimental implementation. System parameters are given in Table II.

A. H-Bridge Inverter With Bipolar PWM-Based GPCC

Performance of the proposed GPCC mimicking bipolar PWM for the control of the single-phase inverter is shown in Fig. 18. In this test, the inverter is injecting 2-A peak current with $\cos(\varphi) = 1$ to the grid when at $t = 0.12$ s $\cos(\varphi)$ changes to 0.5. A similar procedure as per Section III-A is conducted to obtain the current bands for nonunity power factor operation of bipolar PWM-based GPCC. Accordingly, as it can be observed in Fig. 18(a), the current bands are reformed, responding to the step change in $\cos(\varphi)$ at $t = 0.12$ s. It can be seen that the waveforms of the upper and lower bands are not similar to the sinusoidal current but the resulting current spectrum and the average waveform (i_g^{ave}) shows that the output current is stable and free of low-order harmonics. Harmonic spectrum of the grid current is also shown in Fig. 18(a). As it is shown, the proposed method generates a clean output current similar to the original bipolar PWM with the switching harmonics contents concentrated around the switching frequency of 10 kHz.

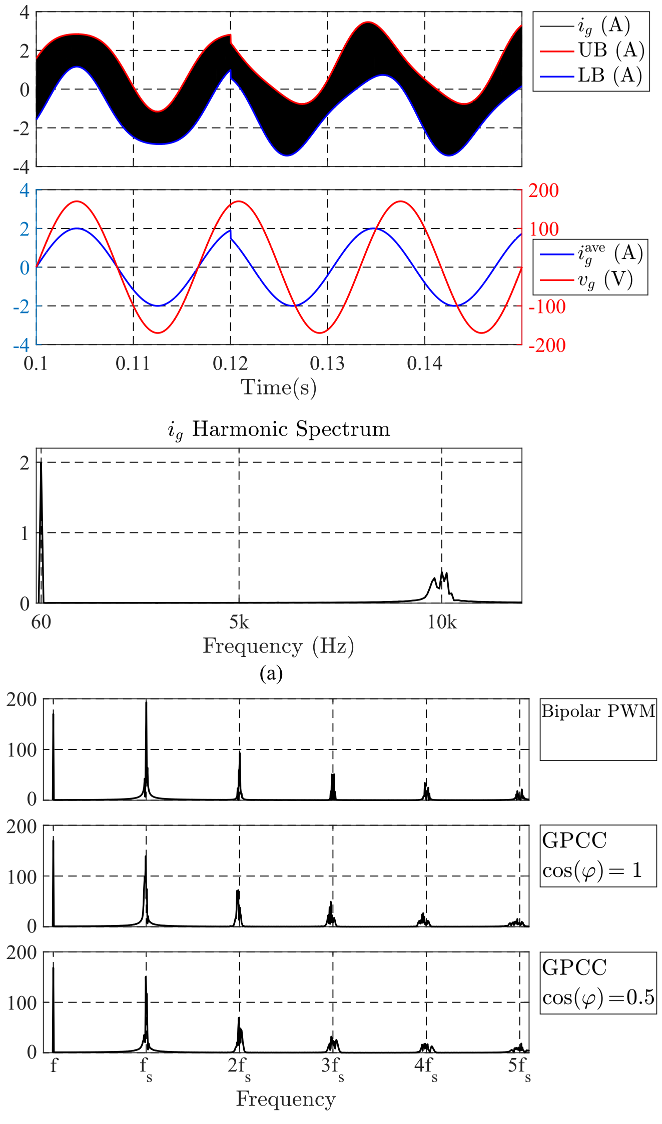

(a)

(b)

Fig. 18. (a) Dynamic performance of the proposed GPCC mimicking bipolar PWM scheme. (b) Inverters' output voltage harmonic spectrum for the original bipolar PWM and the proposed GPCC with two different power factors, $\cos(\varphi) = 1$ and $\cos(\varphi) = 0.5$.

In Fig. 18(b), harmonic spectrum of the inverter controlled with bipolar PWM is compared with that of the proposed GPCC with $\cos(\varphi) = 1$ and $\cos(\varphi) = 0.5$. As it can be observed, with the proposed method for controlling the inverter in nonunity power factors, harmonic spectrum of the output voltage remains similar to that of the original bipolar PWM scheme. Similar to the bipolar PWM, the proposed GPCC has switching frequency components at multiples of the switching frequency f_s and presents a clean output harmonic spectrum.

B. NPC Converter Controlled With the GPCC

Performance of the proposed controller mimicking an IPD modulation for a five-level NPC converter is also evaluated and

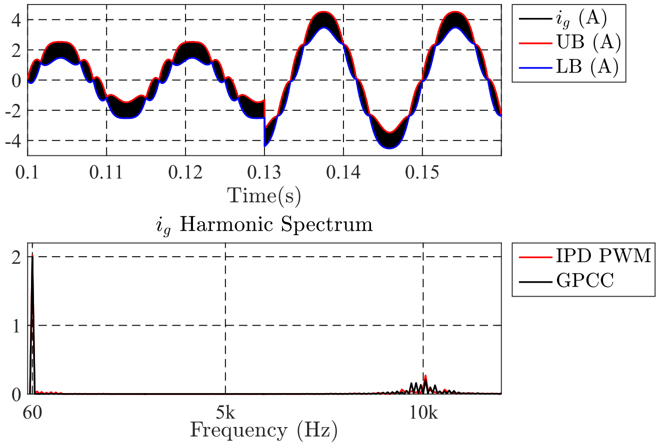

Fig. 19. Dynamic performance of the proposed GPCC mimicking IPD PWM for a five-level NPC converter. Inverter is injecting 170 W to the grid when the reference command jumps to 340 W at $t = 0.13$ s.

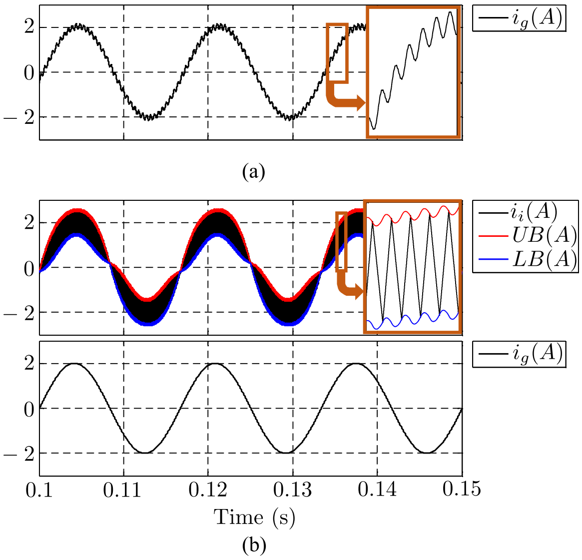

Fig. 20. (a) Grid current for the *LCL* filter case when the active damping branch is disabled. (b) Current of the inverter and grid with the proposed active damping.

results are presented in Fig. 19. The inverter is injecting 2-A peak into the grid when at $t = 0.13$ s the reference command jumps to 4-A peak. As it can be observed, current bands are similar to those derived in Section III-C. FFT analysis results of i_g is also depicted in this figure and it is compared with that of an NPC converter controlled with IPD-PWM. It can be seen that the proposed GPCC presents a similar spectrum and level of harmonics compared with the PWM scheme.

C. H-Bridge Inverter With Unipolar PWM-Based GPCC

The *LCL* filter is simulated with the proposed GPCC mimicking unipolar PWM, while the damping strategy is disabled. Results are shown in Fig. 20(a) where the resonant can be observed on the grid current. In another test, the proposed damping technique is added to the system and results are shown in Fig. 20(b).

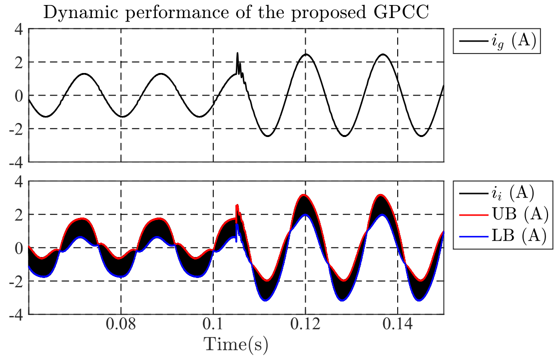

Fig. 21. Dynamic performance evaluation of the proposed GPCC mimicking unipolar PWM with an *LCL* output filter. The inverter is initially injecting 100 W when the reference command jumps to 200 W and 100 VAR at $t = 0.105$ s.

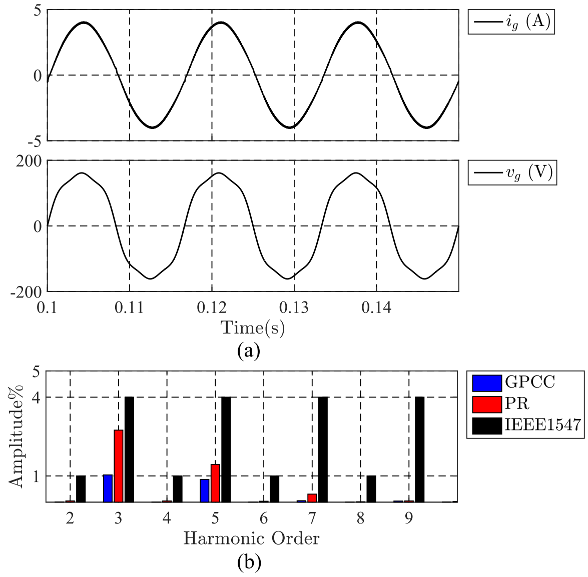

Fig. 22. Steady-state performance of the GPCC with the grid voltage containing 10% third and 5% fifth harmonics. (a) Grid current waveform, (b) harmonic spectrum of the injected grid current and its comparison with the PR controller.

As it can be observed, current bands of i_i are adaptively modified. The bottom plot in Fig. 20(b) shows the effectiveness of the proposed method, as the resonant on the grid current (i_g) is actively damped.

Dynamic performance for *the LCL* filter case with the active damping technique is also evaluated and results are presented in Fig. 21. Peak current reference value in this test jumps from 1 to 3 A at $t = 0.1$ s. As it can be observed, the proposed controller presents a very fast transient response.

Steady-state performance of the controller is also evaluated when it is used in a grid with significant low-order harmonics. The grid voltage in this test has 10% third and 5% fifth harmonics and results are presented in Fig. 22(a). Although the grid is unrealistically polluted with THD $= 11.18\%$, grid current remains sinusoidal with THD $= 1.67\%$. Harmonic spectrum of the grid current is also shown in Fig. 22(b) confirming that harmonics are within IEEE-1547 standard limits [27]. In this

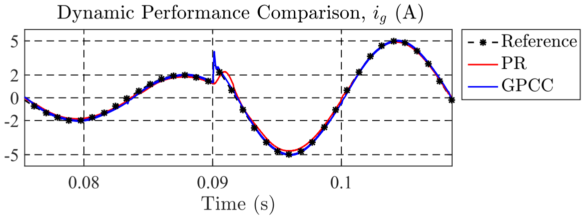

Fig. 23. Dynamic performance comparison of the proposed controller with a PR current controller.

figure, harmonic spectrum of the grid current controlled by a proportional-resonant (PR) controller is also depicted that is discussed in the next section.

Basic structure of the proposed controller regulates the inverter output current within the bands to track the reference. This reference current is affected by the PLL. Therefore, as long as the PLL remains immune to the grid voltage harmonics, the reference current, and thus, the grid current will not be polluted. When the proposed active damping is added as shown in Fig. 15, i_d branch impacts the current in inductor L as well. Consequently, grid harmonics that are projected on v_c, degrade the quality of the output current through i_d. However, rejecting these harmonics through the PLL [25], [28] or by a simple prefiltering of the capacitor voltage solves this problem. A series of cascaded notch filters tuned at low-order harmonics of interest introduces such filtering to the active damping loop, which is employed for the test results of Fig. 22.

D. Comparison With Average Current Controllers

Average current controllers such as proportional-integral and PR controllers are widely used for the control of single-phase grid-connected inverters in renewable energy applications [29], [30]. In this section, performance of the proposed controller is compared with that of a PWM inverter with a PR controller. A step change in the reference current amplitude from 2 to 5 A is applied to both controllers and results are compared in Fig. 23. As it can be observed, the proposed GPCC tracks the reference current with almost no delay, while the PR controller requires about half grid cycle to reach a zero steady-state error for the current.

Steady-state performance of these controllers are also compared when they are integrated in a harmonic polluted grid with 10% third and 5% fifth harmonics. Harmonic controller blocks in the form of several resonant controllers tuned at the harmonic frequencies [31], [32] are added to the PR controller to reject the grid harmonics. Results are depicted in Fig. 22(b) showing that both GPCC and PR controller present adequate steady-state response, satisfying the standard limits.

In conclusion, the proposed controller presents a superior dynamic response with robust performance in comparison with the average current controllers associated with PWM inverters. It is noteworthy that the proposed GPCC achieves such superiority without compromising the fixed switching frequency, clean output voltage spectrum, and the converter loss of PWM inverters.

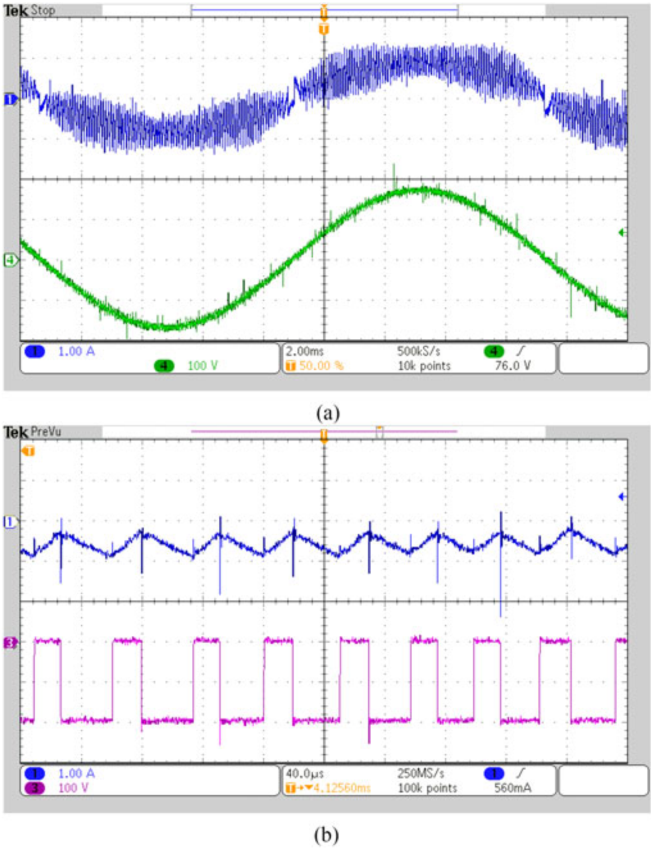

(a)

(b)

Fig. 24. Experimental results. Ch.1: Inverter current (1A/div), Ch.3: Inverter voltage (100 V/div), and Ch.4: Grid voltage (100 V/div). (a) Inverter is injecting 85 W to the grid (2 ms/div). (b) Zoomed snapshot of current and inverter voltage waveforms in this test (40 μs/div).

Regarding practical implementation, the proposed method does not introduce any noticeable complexity to the system. A PWM controller implemented on digital signal processor (DSP) needs the feedbacks to be sampled at least at the rate of output switching frequency. Subsequently, controller calculations are carried out and PWM signals are generated using hardware peripheral of the DSP. Furthermore, the GPCC is concerned with comparing the output current as precisely as possible with the calculated current envelopes to ensure injecting the desired current into the grid. Several low-cost DSPs such as TMS320F28035 [33] from Texas Instruments are commercially available that have on-chip analog comparators well suited for implementation of the GPCC. Accordingly, the analog output current can be compared with digitally calculated bands in such peripheral. In this configuration, current bands can be calculated in a low sampling frequency, e.g., 10 kHz.

E. Experimental Results

The GPCC mimicking bipolar PWM for the control of a single-phase H-Bridge converter is also experimentally validated. System parameters are presented in Table II. Results are shown in Fig. 24(a), where inverter is injecting 85 W to the grid. Output power is set to this low value to better show the effect of double frequency bands on the output current. A zoomed snapshot of output current and inverter voltage is shown in Fig. 24(b).

VI. CONCLUSION

A fixed switching frequency GPCC method for inverters is proposed. While controlling the peak value of the inverters' current, the proposed approach can mimic any known PWM strategy. As a result, the GPCC features all the advantages of peak current and hysteresis controllers, along with a fixed switching frequency and clean and predictable output harmonic spectrum inheriting from the original PWM scheme. Using the proposed method, both concerns of 1) inverters' current control and 2) its desired switching harmonic spectrum will be addressed. The GPCC approach is first proposed for a general case. Then, this method is applied to different PWM schemes such as unipolar and bipolar PWMs to control a single-phase H-Bridge and Z-source inverter and also a multilevel IPD modulation to control an N-level NPC converter. As a result, generality of the proposed method and its ability to implement different PWM schemes and to control different inverter topologies is shown. Moreover, the proposed technique can obtain additional control objectives by its adaptive bands. The GPCC is extended for *LCL*-type output filters for which, an active damping strategy based on adaptive bands of the controller is also proposed. Simulations and experimental results are presented to validate the method.

REFERENCES

[1] C.-H. Chang, F.-Y. Wu, and Y.-M. Chen, "Modularized bidirectional grid-connected inverter with constant-frequency asynchronous sigma-delta modulation," *IEEE Trans. Ind. Electron.*, vol. 59, no. 11, pp. 4088–4100, 2012.

[2] R. Gupta, "Generalized frequency domain formulation of the switching frequency for hysteresis current controlled VSI used for load compensation," *IEEE Trans. Power Electron.*, vol. 27, no. 5, pp. 2526–2535, May 2012.

[3] H. Yi, F. Zhuo, F. Wang, and Z. Wang, "A digital hysteresis current controller for three-level neural-point-clamped inverter with mixed-levels and prediction-based sampling," *IEEE Trans. Power Electron.*, vol. 31, no. 5, pp. 3945–3957, May 2016.

[4] S. Gautam and R. Gupta, "Switching frequency derivation for the cascaded multilevel inverter operating in current control mode using multiband hysteresis modulation," *IEEE Trans. Power Electron.*, vol. 29, no. 3, pp. 1480–1489, Mar. 2014.

[5] C. N.-M. Ho, V. S. Cheung, and H. S.-H. Chung, "Constant-frequency hysteresis current control of grid-connected VSI without bandwidth control," *IEEE Trans. Power Electron.*, vol. 24, no. 11, pp. 2484–2495, Nov. 2009.

[6] F. Blaabjerg, R. Teodorescu, M. Liserre, and A. Timbus, "Overview of control and grid synchronization for distributed power generation systems," *IEEE Trans. Ind. Electron.*, vol. 53, no. 5, pp. 1398–1409, Oct. 2006.

[7] M. Aime, G. Gateau, and T. A. Meynard, "Implementation of a peak-current-control algorithm within a field-programmable gate array," *IEEE Trans. Ind. Electron.*, vol. 54, no. 1, pp. 406–418, Feb. 2007.

[8] T. V. Papathomas, "On the stability of peak current-controlled converters: Analysis, simulation, and experiments," *IEEE Trans. Ind. Electron.*, vol. IE-33, no. 2, pp. 176–184, May 1986.

[9] F. Tian, S. Kasemsan, and I. Batarseh, "An adaptive slope compensation for the single-stage inverter with peak current-mode control," *IEEE Trans. Power Electron.*, vol. 26, no. 10, pp. 2857–2862, Oct. 2011.

[10] H.-S. Youn, J.-S. Park, K.-B. Park, J.-I. Baek, and G.-W. Moon, "A digital predictive peak current control for power factor correction with low-input current distortion," *IEEE Trans. Power Electron.*, vol. 31, no. 1, pp. 900–912, Jan. 2016.

[11] Y.-H. Liao, "A novel reduced switching loss bidirectional ac/dc converter PWM strategy with feedforward control for grid-tied microgrid systems," *IEEE Trans. Power Electron.*, vol. 29, no. 3, pp. 1500–1513, Mar. 2014.

[12] J. Zhao, X. He, and R. Zhao, "A novel PWM control method for hybrid-clamped multilevel inverters," *IEEE Trans. Ind. Electron.*, vol. 57, no. 7, pp. 2365–2373, Jul. 2010.

[13] L. Malesani and P. Tenti, "A novel hysteresis control method for current-controlled voltage-source PWM inverters with constant modulation frequency," *IEEE Trans. Ind. Appl.*, vol. 26, no. 1, pp. 88–92, Jan./Feb. 1990.

[14] L. Malesani, L. Rossetto, and A. Zuccato, "Digital adaptive hysteresis current control with clocked commutations and wide operating range," *IEEE Trans. Ind. Appl.*, vol. 32, no. 2, pp. 316–325, Mar./Apr. 1996.

[15] B. Bose, "An adaptive hysteresis-band current control technique of a voltage-fed PWM inverter for machine drive system," *IEEE Trans. Ind. Electron.*, vol. 37, no. 5, pp. 402–408, Oct. 1990.

[16] C.-S. Lam, M.-C. Wong, and Y.-D. Han, "Hysteresis current control of hybrid active power filters," *IET Power Electron.*, vol. 5, no. 7, pp. 1175–1187, Aug. 2012.

[17] M. Elsaharty, M. Hamad, and H. Ashour, "Digital hysteresis current control for grid-connected converters with LCL filter," in *Proc. 37th Annu. Conf. IEEE Ind. Electron. Soc.*, Nov. 2011, pp. 4685–4690.

[18] T. Kerekes, R. Teodorescu, and U. Borup, "Transformerless photovoltaic inverters connected to the grid," in *Proc. IEEE 22nd Annu. Appl. Power Electron. Conf.*, Feb. 2007, pp. 1733–1737.

[19] C. N.-M. Ho, V. S. Cheung, and H. S.-H. Chung, "Constant-frequency hysteresis current control of grid-connected VSI without bandwidth control," *IEEE Trans. Power Electron.*, vol. 24, no. 11, pp. 2484–2495, Nov. 2009.

[20] M. A. Rahman, T. Radwan, A. Osheiba, and A. Lashine, "Analysis of current controllers for voltage-source inverter," *IEEE Trans. Ind. Electron.*, vol. 44, no. 4, pp. 477–485, Aug. 1997.

[21] B. Wu, *High-Power Converters and AC Drives*. New York, NY, USA: Wiley, 2006.

[22] F. Z. Peng, "Z-source inverter," *IEEE Trans. Ind. Appl.*, vol. 39, no. 2, pp. 504–510, Mar./Apr. 2003.

[23] O. Husev, A. Chub, E. Romero-Cadaval, C. Roncero-Clemente, and D. Vinnikov, "Hysteresis current control with distributed shoot-through states for impedance source inverters," *Int. J. Circuit Theory Appl.*, vol. 44, no. 4, pp. 783–797, 2015.

[24] M. Shen and F. Z. Peng, "Operation modes and characteristics of the z-source inverter with small inductance or low power factor," *IEEE Trans. Ind. Electron.*, vol. 55, no. 1, pp. 89–96, Jan. 2008.

[25] M. Karimi-Ghartemani, "Linear and pseudolinear enhanced phased-locked loop (EPLL) structures," *IEEE Trans. Ind. Electron.*, vol. 61, no. 3, pp. 1464–1474, Mar. 2014.

[26] M. Ciobotaru *et al.*, "A new single-phase PLL structure based on second order generalized integrator," in *Proc. Power Electron. Spec. Conf.*, 2006, pp. 1–6.

[27] *IEEE-1547 Standard for Interconnecting Distributed Resources with Electric Power Systems*, IEEE Standard 1547, Jul. 2003.

[28] M. Karimi-Ghartemani, S. A. Khajehoddin, P. Jain, and A. Bakhshai, "Comparison of two methods for addressing dc component in phase-locked loop (PLL) systems," in *Proc. 2011 IEEE Energy Convers. Congr. Expo.*, 2011, pp. 3053–3058.

[29] M. Ebrahimi, S. A. Khajehoddin, and M. Karimi-Ghartemani, "Fast and robust single-phase current controller for smart inverter applications," *IEEE Trans. Power Electron.*, vol. 31, no. 5, pp. 3968–3976, May 2016.

[30] S. A. Khajehoddin, A. Bakhshai, P. Jain, and J. Drobnik, "A robust power decoupler and maximum power point tracker topology for a grid-connected photovoltaic system," in *Proc. 2008 IEEE Power Electron. Spec. Conf.*, 2008, pp. 66–69.

[31] S. Khajehoddin, M. Karimi-Ghartemani, A. Bakhshai, and P. Jain, "High quality output current control for single phase grid-connected inverters," in *Proc. 2014 IEEE Appl. Power Electron. Conf. Expo.*, 2014, pp. 1807–1814.

[32] M. Karimi-Ghartemani, S. A. Khajehoddin, P. Jain, and A. Bakhshai, "Linear quadratic output tracking and disturbance rejection," *Int. J. Control*, vol. 84, no. 8, pp. 1442–1449, 2011.

[33] *TMS320F2803x Piccolo Microcontrollers*, Texas Instruments, Dallas, TX, USA, Jun. 2016.

Mohammad Ebrahimi (S'11) received the B.Sc. and M.Sc. degrees from the Isfahan University of Technology, Isfahan, Iran, in 2010 and 2013, both in electrical power engineering. He is currently working toward the Ph.D. degree in electrical engineering with the University of Alberta, Edmonton, Canada.

His research interest includes power electronics applications in power and renewable energy systems and high-power-density converters.

S. Ali Khajehoddin (S'04–M'10–SM'16) received the B.Sc. and M.Sc. degrees in electrical engineering from the Isfahan University of Technology, Isfahan, Iran, and the Ph.D. degree in electrical engineering specialized in power electronics and their applications in renewable energy systems from Queen's University, Kingston, Canada, in April 2010.

After completing his Master's, he cofounded a start-up company, which was focused on the development and production of power analyzers and smart metering products used for smart grid applications. For his doctoral research at Queen's University, he focused on the design and implementation of compact and durable microinverters for photovoltaic (PV) grid-connected systems. Based on this research, Queen's University spun off SPARQ systems, Inc., where, as the Lead R&D Engineer, he worked toward mass-production and commercialization of microinverters from 2010 to 2013. He joined the Department of Electrical and Computer Engineering, University of Alberta, Edmonton, Canada, in 2013.

Dr. Khajehoddin is an Associate Editor of the IEEE TRANSACTION ON SUSTAINABLE ENERGY and IEEE TRANSACTIONS ON POWER ELECTRONICS.